Liquid Crystals
Publication details, including instructions for authors and subscription information:
http://www.informaworld.com/smpp/title~content=t713926090

Landau-de Gennes modelling of nematic liquid crystal colloids

Miha Ravnik[a]; Slobodan Žumer[ab]
[a] Faculty of Mathematics and Physics, University of Ljubljana, Ljubljana, Slovenia [b] J. Stefan Institute, Ljubljana, Slovenia

First published on: 08 October 2009

To cite this Article Ravnik, Miha and Žumer, Slobodan(2009) 'Landau-de Gennes modelling of nematic liquid crystal colloids', Liquid Crystals, 36: 10, 1201 — 1214, First published on: 08 October 2009 (iFirst)
To link to this Article: DOI: 10.1080/02678290903056095
URL: http://dx.doi.org/10.1080/02678290903056095

Liquid Crystals,
Vol. 36, Nos. 10–11, October–November 2009, 1201–1214

Taylor & Francis
Taylor & Francis Group

INVITED ARTICLE

Landau–de Gennes modelling of nematic liquid crystal colloids

Miha Ravnik[a] and Slobodan Žumer[a,b]*

[a]*Faculty of Mathematics and Physics, University of Ljubljana, Jadranska 19, 1000 Ljubljana, Slovenia;* [b]*J. Stefan Institute, Jamova 39, 1000 Ljubljana, Slovenia*

(Received 16 April 2009; final form 11 May 2009)

Phenomenological Landau–de Gennes modelling based on the free energy of nematic liquid crystal colloids is reviewed. Nematic phase, gradient of order, and surface anchoring contributions to the total free energy are used. The numerical finite difference relaxation technique is explained as an efficient tool for the minimisation of the free energy. Effects of the mesh and mesh allocation are discussed. Various conceptually different colloidal structures are calculated to show the universality of the model. Single particles, dipolar–quadrupolar dimers, entangled dimers, dimers bound by escaped hyperbolic rings, and hierarchically patterned Saturn-ring colloidal superstructures are presented.

Keywords: Landau–de Gennes free energy; colloids; liquid crystal; modelling; structures

1. Introduction

Liquid crystal colloids are materials characterised by the anisotropy of the liquid crystalline continuum phase (*1*, *2*) and discrete ordering of dispersed colloidal inclusions. The long-ranged orientational ordering of liquid crystals generates structural forces between the colloidal inclusions which allow the assembly of complex colloidal composites. The binding energies of inclusions in liquid crystals are a few orders of magnitude higher as compared with water-based colloids. The inherent effective elasticity of liquid crystals permits structuring of the inclusions based on hierarchical ordering (*3*, *4*) and self-assembly (*5*). The primary interest in liquid crystal colloids is related to their applications in optics (*6*, *7*), where the complex anisotropic properties of liquid crystals are combined with the optical response of colloidal dispersions.

Colloidal particles immersed in a liquid crystal host interact with the surrounding liquid crystal primarily through surface anchoring (*8*). The surface anchoring perturbs the orientation of the liquid crystal, i.e. the director **n**, by imposing the preferential orientation at the particle walls. Such perturbation usually has a dipolar or quadrupolar symmetry, and particles together with the perturbation are often referred to as elastic dipoles or quadrupoles (*9*). Elastic dipoles and quadrupoles of particles with homeotropic (perpendicular) surface anchoring are characterised by −1 hyperbolic point defects or $-1/2$ disclination Saturn-ring defects, respectively (*10*). Particles with planar surface anchoring have quadrupolar symmetry and generate two $-1/2$ 'boojum' surface defects. The symmetry and the structure of the director field around particles is determined by the surface anchoring strength, particle size, confinement and external fields (*11*).

Particles dispersed in a liquid crystal host are subjected to long-range interparticle structural forces. These are thermodynamic forces and their source at the molecular scale are van der Waals intermolecular interactions. At the particle scale, however, single molecular contributions typically smear out and the liquid crystal effectively acts as an elastic medium trying to retain the orientational order of its molecules. At these scales, structural forces are therefore considered as effective elastic forces which try to minimise the perturbation of the director field induced by inclusions. The profile of structural forces is typically highly anisotropic and is governed by the geometry of the system and symmetry of the director field. The complex interactions between inclusions in liquid crystals lead to complex relaxations in colloidal dispersions that give rise to numerous colloidal structures.

In recent years, assisted and true self-assembly has been observed for various colloidal structures. The first observed liquid crystal colloidal structures were chains of elastic dipoles (*1*, *12*, *13*). The assembly of dipolar chains at a larger length scale was realised by phase separation in a binary mixture of silicone oil and nematic liquid crystal (*14*). Dipolar chain segments were further observed to build complex two-dimensional (2D) cluster aggregates (*15*, *16*). Quadrupolar particles in a nematic were observed to form kinked chains (*17*). Only recently have the assembly of regular 2D colloidal crystals of elastic dipoles, quadrupoles and their combination

*Corresponding author. Email: slobodan.zumer@fmf.uni-lj.si

ISSN 0267-8292 print/ISSN 1366-5855 online

DOI: 10.1080/02678290903056095
http://www.informaworld.com

been demonstrated (*18–20*). At the interfaces, 2D hexagonal ordering of glycerol droplets has been observed (*21–23*). In addition, it was reported on particle-stabilised gels in a cholesteric liquid crystal (*24*), orientational ordering of magnetic nanowires in a nematic (*25*), combined charge and nematic stabilisation of a colloidal dispersion (*26*), helical self-ordering of cellulose microfibrils (*27*), photonic band study in nematic solutions (*28*), and laser tweezers measurements of interparticle interactions in nematic liquid crystal (*16*, *29*, *30*).

Depending on the size and typical scale of a considered system, the theory and modelling of liquid crystal colloids rely on molecular, effective molecular or phenomenological approaches (*31–34*). These approaches are complemented by a topological approach that takes into account the symmetries of nematic liquid crystals. Via topological conservation rules, topology allows predictions of the general features of defect-mediated colloidal particle assemblies. Molecular approaches provide insight into the detailed structure of defects, explain the role of the thermal fluctuations, and allow modelling of truly nano-sized inclusions. At experimentally accessible micrometre scales, it is convenient to use phenomenological mean-field approaches based on the minimisation of the free energy that is obtained by the expansion in terms of a mesoscopic order parameter. This is usually called the Landau–de Gennes (LdG) free energy and is characterised by a few phenomenological material constants that rely on experiments. In general, LdG modelling leads to only a few analytical solutions so numerical methods such as relaxation techniques with finite differences or finite elements and lattice Boltzmann algorithms are commonly used (*35–37*). For complex systems such as liquid crystal colloids, theoretical studies are particularly useful, since they cover a large spectra of material parameters and can thus be used to search for and predict new structures.

The LdG free energy approach can be used in unrestricted and confined liquid crystal geometries. In particular, it is useful in multi-particle colloidal systems when the particles are at close distances and generate defects in the liquid crystalline order. The inherent possibility to incorporate defects also allows for modelling of the defects with higher topological charges and higher winding numbers (*38*, *39*). The dynamics of particles within LdG modelling is typically described in terms of quasi-dynamics. Approaches have been proposed that use true nematodynamics, yet they are typically demanding and require different methods to locate the particles (*40*, *41*). Including chirality within the LdG framework is achieved by extending the free energy functional with additional phenomenological terms. This generalised LdG free energy can be used for modelling of inhomogeneous cholesteric and blue phases (*42*, *43*).

In this review we show how one can use the LdG phenomenological free energy in modelling nematic liquid crystal colloids. The basic characteristics of the numerical modelling are addressed. Colloidal configurations with single elastic dipoles and quadrupoles, entangled dimers and dimers with escaped hyperbolic rings are presented. Hierarchical ordering of smaller sub-micrometre particles into a Saturn ring of a micrometre-sized particle is also shown.

2. LdG modelling

In this section we introduce the main features of this phenomenological approach. Particular emphasis is placed on the nematic order parameter, control of the nematic degree of order, nematic liquid crystal elasticity and surface anchoring functionals. Finally, the numerical finite difference relaxation method is discussed.

2.1 Nematic order parameter

The long-range orientational order of the molecules is the central phenomenon which makes liquid crystals unique compared with, for example, solid crystals. It can continuously vary at scales from nanometres to micrometres and is typically highly responsive to external fields. In confined geometries, opposing orientational ordering of different surfaces can lead to the formation of defect regions, where the orientation of the molecules is undefined. In nematic liquid crystals, the defects are either lines or points (*44*).

A nematic liquid crystal requires a tensorial order parameter field Q_{ij} to characterise all of its orientational degrees of freedom: orientation of the director (two angles), orientation of the possible biaxial ordering relative to the director (one angle), nematic degree of order S and biaxiality P. The director $\mathbf{n}(\mathbf{r}, t)$, describes the average orientation of nematic molecules at a given position $\mathbf{r}$ at time t, with orientations $\mathbf{n}(\mathbf{r}, t) \rightarrow -\mathbf{n}(\mathbf{r}, t)$ being equivalent. More precisely, the director is given as the ensemble average of molecular orientations within a given volume segment or, due to ergodicity, as the time average of a single molecule orientation at a given position. Orientational fluctuations of the molecules around the director are quantified by the nematic degree of order S, which is defined as an ensemble average of the second Legendre polynomials evaluated for the dot product between the molecular orientations and the director. The values of S lie in the interval $[-\frac{1}{2}, 1]$: $S = 1$ corresponds to a perfect nematic order, $S = 0$ characterises a completely disordered (isotropic) state, and $S = -\frac{1}{2}$ determines perfect molecular ordering within the plane perpendicular to $\mathbf{n}$. It is common for nematic orientational order to become biaxial if

external fields (e.g. surface, electric, magnetic) break the rotational symmetry of the molecular orientational fluctuations around the director. Values of the biaxiality parameter P lie in the interval $[-\frac{3}{2}, \frac{3}{2}]$, where $P = 0$ characterises uniaxial ordering and $|P| = \frac{3}{2}$ corresponds to the perfect biaxial ordering along the secondary director $\mathbf{e}^{(1)}$ which is perpendicular to $\mathbf{n}$. In general, the order parameter tensor Q_{ij} reads

$$Q_{ij} = \frac{S}{2}(3n_i n_j - \delta_{ij}) + \frac{P}{2}\left(e_i^{(1)} e_j^{(1)} - e_i^{(2)} e_j^{(2)}\right), \qquad (1)$$

where $\mathbf{e}^{(2)} = \mathbf{n} \times \mathbf{e}^{(1)}$. By definition, the tensor Q_{ij} is symmetric and traceless. Its largest eigenvalue is the nematic degree of order S and the corresponding eigenvector the director $\mathbf{n}$. The other two eigenvalues are equal to $-\frac{1}{2}(S + P)$ and $-\frac{1}{2}(S - P)$ with the corresponding eigenvectors $\mathbf{e}^{(1)}$ and $\mathbf{e}^{(2)}$, respectively. In the case of uniaxial nematics that are only weakly deformed, we have $S = constant$ and $P = 0$.

2.2 Nematic–isotropic transition

For most liquid crystal materials, the stability of the nematic mesophase depends either on temperature or on molecular concentration. In this work, we are interested in thermotropic liquid crystals, where the temperature determines the liquid crystalline mesophase. The nematic–isotropic (NI) phase transition relevant for our work is discontinuous (first order).

An established approach to model the NI transition is to use the invariants of the nematic order parameter tensor and construct Landau expansion of the free energy. The free energy volume density f_{phase} with minimum number of terms needed to model the NI transition reads (*1*):

$$f_{\text{phase}} = \frac{1}{2}a(T - T^*_{\text{NI}})Q_{ij}Q_{ji} + \frac{1}{3}BQ_{ij}Q_{jk}Q_{ki} + \frac{1}{4}C(Q_{ij}Q_{ji})^2, \qquad (2)$$

where a, B and C are nematic material parameters, T is temperature and T^*_{NI} is the supercooling temperature. Typical values for the material parameters are $a \sim 10^5 \text{J}m^{-3}K^{-1}$, $B \sim -10^6 \text{J}m^{-3}$ and $C \sim 10^6 \text{J}m^{-3}$. In the nematic phase both the first and second prefactor in the expansion are negative and only $C > 0$ ensures that the free energy density functional is bounded from below. Unlike the constants B and C, the first prefactor $a(T - T^*_{\text{NI}})$ is temperature dependent and therefore drives the NI transition. We note that if nematic materials are intrinsically biaxial, a Landau expansion that also includes sixth-order terms has to be constructed (*45*).

Free energy functional which drives the NI transition in terms of the uniaxial nematic order can be obtained from Equation (2) by assuming uniaxial ordering of the nematic $[Q^{\text{U}}_{ij} = S(3n_i n_j - \delta_{ij})/2]$. Trace invariants of the uniaxial order parameter tensor simplify as $Q^{\text{U}}_{ij}Q^{\text{U}}_{ji} = 3S^2/2$ and $Q^{\text{U}}_{ij}Q^{\text{U}}_{jk}Q^{\text{U}}_{ki} = 3S^3/4$. Rewriting f_{phase} in terms of S one finds:

$$f_{\text{phase}} = \frac{3}{4}a(T - T^*_{\text{NI}})S^2 + \frac{1}{4}BS^3 + \frac{9}{16}CS^4. \qquad (3)$$

It is now easy to interpret the role of all three Landau expansion terms: the first term drives the transition, the second term ensures asymmetry of S by breaking the S to $-S$ invariance, and the third term bounds the values of S from below. The equilibrium nematic degree of order S_{eq} is found by minimising the corresponding free energy $F_{\text{ORD}} = \int f_{\text{phase}} \text{d}V$. The minimisation gives

$$S_{\text{eq}} = \begin{cases} 0, & T > T_{\text{NI}} \\ \frac{1}{2}\left[-B/3C + \sqrt{(B/3C)^2 - 8a(T - T^*_{\text{NI}})/3C}\right], & T < T_{\text{NI}} \end{cases}$$

where T_{NI} is the NI transition temperature. The supercooling temperature T^*_{NI}, NI transition temperature T_{NI} and the super-heating temperature T^{**}_{NI} are related via material parameters as $T_{\text{NI}} = T^*_{\text{NI}} + B^2/27aC$ and $T^{**}_{\text{NI}} = T^*_{\text{NI}} + B^2/24aC$.

2.3 Gradient of order and nematic elasticity

Nematic materials act as effective elastic materials if their orientational ordering is subjected to spatial variations. Phenomenologically, in a similar manner as for the nematic degree of order, a free energy functional is constructed from the scalar invariants of the order parameter tensor to penalise the elastic distortions. Free energy terms are usually second order in derivatives and satisfy the inversion symmetry for the non-chiral materials. A common approximation to simplify the free energy density functional is to use one elastic constant approximation. The gradient free energy f_{grad} within the one-constant approximation reads

$$f_{\text{grad}} = \frac{1}{2}L\frac{\partial Q_{ij}}{\partial x_k}\frac{\partial Q_{ij}}{\partial x_k}, \qquad (4)$$

where L is the single elastic constant, x_i are Cartesian coordinates and summation over repeated indices is assumed. If the system is uniaxial, the gradient free energy (Equation (4)) can be rewritten in terms of the director $\mathbf{n}$ and nematic degree of order S as

$$f_{\text{grad}} = \frac{1}{2}K(\nabla \mathbf{n})^2 + \frac{3}{4}L(\nabla S)^2, \qquad (5)$$

where the single Frank elastic constant $K = 9LS^2/2$. Note that the first term in Equation (5), which

characterises the director elasticity, differs from the standard Frank elastic term $K[(\nabla \cdot \mathbf{n})^2 + (\nabla \times \mathbf{n})^2]/2$ by a surface term (*1*). The suitability of the one-constant approximation is highly dependent on the material. In general, any elastic deformation can be decomposed into three basic deformation modes, splay, twist and bend (*1*). For 5CB nematic, the splay, bend and twist elastic constants differ from the average value $K = 6 \times 10^{-12}$N by around 40% (see (*46*)).

To incorporate the three basic deformation modes, the free energy density is expanded into three terms with the corresponding elastic constants L_1, L_2 and L_3. Such generalised formulation of the elastic free energy volume density f_{grad} commonly reads (*47–49*)

$$f_{\text{grad}} = \frac{1}{2} L_1 \frac{\partial Q_{ij}}{\partial x_k} \frac{\partial Q_{ij}}{\partial x_k} + \frac{1}{2} L_2 \frac{\partial Q_{ij}}{\partial x_j} \frac{\partial Q_{ik}}{\partial x_k} + \frac{1}{2} L_3 Q_{ij} \frac{\partial Q_{kl}}{\partial x_i} \frac{\partial Q_{kl}}{\partial x_j}. \quad (6)$$

The L_i are independent of the nematic degree of order and should be interpreted as the direct strength of the inter-molecular interactions. In general, a more complex elastic free energy functional constructed from scalar invariants of the order parameter tensor is allowed by symmetry (*50*).

Elastic free energy f_{grad} based on the order parameter tensor is rewritten for a uniaxial nematic in terms of the director field $\mathbf{n}$ (see (*51*)). Using $Q_{ij}^{\text{U}} = S(3n_i n_j - \delta_{ij})/2$, $n_i n_i = 1$ and $n_i(\partial n_i/\partial x_k) = 0$ the elastic free energy density in the standard Frank–Oseen form $f_{\text{grad}}^{\text{FO}}$ reads as:

$$f_{\text{grad}}^{\text{FO}} = \frac{1}{2} K_1 (\nabla \cdot \mathbf{n})^2 + \frac{1}{2} K_2 [\mathbf{n} \cdot (\nabla \times \mathbf{n})]^2 + \frac{1}{2} K_3 [\mathbf{n} \times (\nabla \times \mathbf{n})]^2, \quad (7)$$

where K_i are Frank elastic constants given as combinations of L_i: $L_1 = (K_3 + 2K_2 - K_1)/9S^2$, $L_2 = 4(K_1 - K_2)/9S^2$ and $L_3 = 2(K_3 - K_1)/9S^3$. The constants K_i incorporate the degree of nematic order as an internal parameter and are proportional to S^2. The possible advantage of using K_i set of constants instead of L_i, is that they characterise basic deformation modes directly: K_1 splay, K_2 twist and K_3 bend deformation. The Frank–Oseen free energy can be extended by the divergence free energy density terms f_{13} (see (*52*)) and f_{24} (see (*53*)) allowed by the symmetry.

Chiral nematic materials are modelled by including pseudoscalar phenomenological terms in the total free energy. Chirality of the material is characterised by the pitch p_0 of the helix that forms when the material is in the cholesteric phase. Such a chiral gradient free energy density reads within a single elastic approximation as (*54*)

$$f_{\text{grad}}^{\text{chiral}} = \frac{L}{2} \frac{\partial Q_{ij}}{\partial x_k} \frac{\partial Q_{ij}}{\partial x_k} + 2q_0 L \varepsilon_{ikl} Q_{ij} \frac{\partial Q_{lj}}{\partial x_k}, \quad (8)$$

where q_0 is a chiral parameter related to the pitch of the cholesteric helix by $p_0 = 2\pi/q_0$ and ε_{ikl} is the fully antisymmetric alternating tensor equal to +1 (–1) if i, k, l is an even (odd) permutation of $1, 2, 3$ and zero otherwise. We should comment that the above chiral gradient free energy (Equation (8)) not only applies for cholesteric phases, but can also be used to model cholesteric blue phases (*42*, *43*).

2.4 LdG free energy

The elastic free energy f_{grad} and the free energy characterising the nematic degree of order f_{phase} constitute the LdG free energy when combined into a single functional. Denoting the total LdG free energy volume density as f_{LdG} one can write

$$f_{\text{LdG}} = f_{\text{grad}} + f_{\text{phase}}. \quad (9)$$

The LdG approach allows phenomenological modelling of the nematic liquid crystals at the micrometre and sub-micrometre mesoscale as it incorporates both nematic elasticity and spatial variation of the nematic degree of order. It can be applied for arbitrary geometries, different length scales and is easily extendable to include the effects of external fields. The only inherent limitation of the LdG model is that it becomes less reliable at nanometre scales because of its mean-field character. The order parameter tensor used as the main element of the model namely assumes an ensemble average of molecular orientations, which are typically a few nanometres in length. Detailed effects at true nanometre scales are therefore more properly accessed by molecular approaches, such as the Gay–Berne potential-based Monte Carlo studies (*55*).

The ratio of the two energy contributions in LdG free energy introduces a characteristic length scale, referred to as nematic correlation length ξ_{N}. To extract ξ_{N} from f_{LdG}, we rewrite the free energy density f_{LdG} within the one-elastic-constant approximation using uniaxial order parameter tensor Q_{ij}^{U} and assuming spatial variations of S alone ($\nabla S \neq 0$, $\nabla \mathbf{n} = 0$)

$$f_{\text{LdG}} = \frac{3}{4} a(T - T_{\text{NI}}^*) S^2 + \frac{1}{4} B S^3 + \frac{9}{16} C S^4 + \frac{3}{4} L (\nabla S)^2. \quad (10)$$

Minimising Equation (10) with the Euler–Lagrange (EL) formalism one obtains

$$\frac{3}{2}L\nabla^2 S - \frac{\partial f_{\mathrm{LdG}}}{\partial S} = 0. \qquad (11)$$

Linearising the EL equation (11) for small spatial perturbations from the equilibrium, $S(x_i) = S_{\mathrm{eq}} + \Delta S(x_i)$, the nematic correlation length is obtained:

$$\xi_{\mathrm{N}} = \sqrt{\frac{3}{2}\frac{L}{(\partial^2 f_{\mathrm{LdG}}/\partial S^2)|_{S_{\mathrm{eq}}}}} = \sqrt{\frac{L}{a(T - T^*_{\mathrm{NI}}) + BS_{\mathrm{eq}} + \frac{9}{2}CS_{\mathrm{eq}}}}. \qquad (12)$$

The physical interpretation of ξ_{N} is that it determines the spatial scale for the variation of the nematic degree of order. Its role in nematics is most pronounced in defects as it roughly determines their size. Here ξ_{N} is also the central parameter which controls the mesh resolution in numerical calculations. Typically, ξ_{N} is of the order of a few nanometres.

To show the role of S, P and the components of Q_{ij} in real systems, an example of their spatial profile for an elastic quadrupole is presented in Figure 1. The calculations were performed with $1\mu m$ homeotropic particles in a uniform cell. Further details of the numerical modelling are presented in the following sections. One can nicely see the changes in S and P in the region where the curves pass through the Saturn-ring defect. Components of Q_{ij} also only vary close to the particle, whereas further away they converge to a constant value denoting uniform ordering. Here S and P are calculated from trace invariants of the order parameter tensor by solving the set of equations $\mathrm{tr}(Q_{ij}Q_{ji}) = (3S^2 + P^2)/2$ and $\mathrm{tr}(Q_{ij}Q_{jk}Q_{ki}) = 3S(S^2 - P^2)/4$.

As an internal scale of the nematic liquid crystal, the nematic correlation length in general does not allow for scaling of a given colloidal geometry, cell thickness, particle size or surface anchoring. Yet scaling can be applied in systems where the total free energy consists primarily of the elastic (Frank's) contribution and Landau's contribution due to the variation of the degree of order is small. Modelling with the order parameter tensor is then roughly equivalent to the modelling with the vectorial director field, which is scale-less. Usually scaling approximation holds in systems with no or very localised defects. Scaling can also be nicely applied in colloidal structures with defects that have escaped core regions.

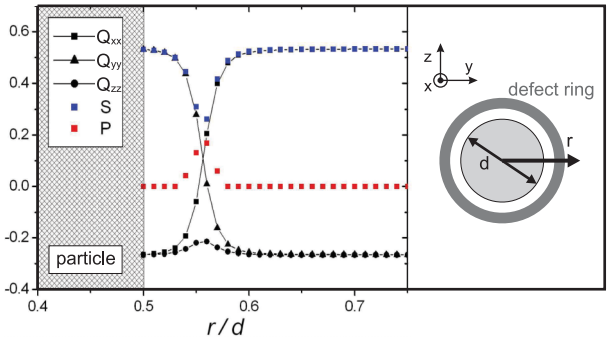

Figure 1. Spatial profiles in the fixed Cartesian coordinate frame Q_{xx}, Q_{yy}, Q_{zz}, degree of order S and biaxiality P. At $r \sim 0.56d$ curves pass through the ring defect and both S and P exhibit strong changes. For $r/d > 0.6$ the field becomes uniform: S = constant, $P = 0$ and Q_{ij} = constant.

An external electric field couples with the nonpolar nematic through a dielectric interaction with the induced dipoles of the nematic molecules. These dipoles are oriented either parallel or perpendicular to the director, depending on the polarisability of nematic molecules with either positive or negative dielectric anisotropy ε_a. Within the LdG framework, the dielectric coupling is introduced as an additional free energy density contribution f_{EM} (*1*, *56*):

$$f_{\mathrm{EM}} = -\frac{1}{2}\varepsilon_0\left(\bar{\varepsilon}E_i^2 + \frac{2}{3}\varepsilon_a^{\mathrm{mol}}Q_{ij}E_iE_j\right), \qquad (13)$$

where ε_0 is the dielectric vacuum permittivity constant, $\bar{\varepsilon} = (2\varepsilon_\perp + \varepsilon_\parallel)/3$ is the average liquid crystal permittivity, $\varepsilon_a^{\mathrm{mol}} = \varepsilon_\parallel^{\mathrm{mol}} - \varepsilon_\perp^{\mathrm{mol}}$ is the molecular dielectric anisotropy (the macroscopic dielectric anisotropy reads as $\varepsilon_a = S\varepsilon_a^{\mathrm{mol}}$), and E_i is the external electric field. Eigenvalues of the molecular dielectric permittivity tensor $\varepsilon_\perp^{\mathrm{mol}}$ and $\varepsilon_\parallel^{\mathrm{mol}}$ correspond to eigenvectors perpendicular and parallel to the director, respectively. Dielectric coupling in Equation (13) requires a true local electric field, therefore in a most general approach Maxwell's equations also have to be solved in accordance with the equations for the order parameter tensor to obtain the equilibrium profile of the nematic.

2.5 *Surface anchoring*

Interfaces with various materials affect liquid crystal ordering by imposing a preferred degree of order and a preferred molecular orientation. Such behaviour is usually referred to as anchoring (*8*). The most common types of anchoring are planar and perpendicular (homeotropic) ordering with respect to the surface.

Within the LdG framework, the uniform surface anchoring is typically modelled by using a Rapini–Papoular-like surface free energy density functional $f_{\mathrm{surf}}^{\mathrm{uni}}$:

$$f_{\text{surf}}^{\text{uni}} = \frac{1}{2} W^{\text{uni}} (Q_{ij} - Q_{ij}^0)^2, \quad (14)$$

where W^{uni} is the uniform surface anchoring strength and Q_{ij}^0 is the surface-preferred order parameter tensor. Here $f_{\text{surf}}^{\text{uni}}$ penalises quadratically all deviations of Q_{ij} from Q_{ij}^0. Therefore, Q_{ij}^0 imposes not only the preferred direction at the surface, the easy axis, but also the surface degree of order and biaxiality. Typically, values for W^{uni} range from 10^{-3} to 10^{-7}Jm^{-2} (see (*57*)), where 10^{-3}–10^{-4}Jm^{-2} is considered strong anchoring and 10^{-6}–10^{-7}Jm^{-2} is considered weak anchoring.

Surfaces with planar anchoring can impose not only uniform but also degenerate surface ordering where molecules prefer to lie in a plane with no in-plane preferred direction. Such anchoring, degenerate in the polar angle, can be incorporated into numerical calculations by using a new degenerate surface potential $f_{\text{surf}}^{\text{deg}}$. Such a degenerate surface functional was introduced by Fournier and Galatola (*58*):

$$f_{\text{surf}}^{\text{deg}} = W_1^{\text{deg}} (\tilde{Q}_{ij} - \tilde{Q}_{ij}^{\perp})^2 + W_2^{\text{deg}} (\tilde{Q}_{ij}\tilde{Q}_{ij} - 9S_S^2)^2, \quad (15)$$

where W_1^{deg} and W_2^{deg} are two surface anchoring constants, S_S is the surface-preferred degree of order, $\tilde{Q}_{ij} = Q_{ij} + S_{\text{eq}}\delta_{ij}/2$, and $\tilde{Q}_{ij}^{\perp}$ is defined using surface normal ν_i as follows:

$$\tilde{Q}_{ij}^{\perp} = P_{ik}\tilde{Q}_{kl}P_{lj}; \quad P_{ij} = \delta_{ij} - \nu_i\nu_j. \quad (16)$$

In Equation (15) the first term is constructed using surface projections P_{ij} and imposes only orientational in-plane ordering with ν_i as the plane normal. The second term determines the surface degree of order by imposing a quadratic potential for S^2.

The strength of the uniform surface anchoring can be interpreted in terms of Kleman–de Gennes extrapolation length ξ_S (see (*59*, *60*)). It is introduced as $\xi_S = K/W^{\text{uni}}$ (where K is the effective Frank elastic constant) and measures relative strength of nematic elasticity with respect to the surface anchoring. Extrapolation lengths of surfaces with strong anchoring ($W^{\text{uni}} \sim 10^{-3}\text{Jm}^{-2}$) are for a typical nematic ($K \sim 10^{-11}\text{N}$) at the order of 10nm as for surfaces with weak anchoring ($W^{\text{uni}} \sim 10^{-6}\text{Jm}^{-2}$) $\xi_S \sim 10\mu\text{m}$.

2.6 Numerical minimisation technique

The LdG free energy density and surface anchoring functionals are the central elements that govern the dynamical evolution and equilibrium configurations of nematic colloids. Using the free energy density terms to construct the total free energy F as $F = \int f \, \text{d}V$ one builds a thermodynamical potential which drives the system towards stable or metastable solutions. An absolute minimum in the free energy corresponds to the equilibrium state, whereas possible higher-value minima give metastable configurations. The typical scale for the free energy changes in nematic colloids with micrometre-sized particles are around 100–10,000 $k_{\text{B}}T$ (where T is temperature).

The total free energy is minimised by using the EL algorithm. EL equations for bulk and surface of the nematic read as

$$\frac{\partial f}{\partial Q_{ij}} - \nabla \frac{\partial f}{\partial \nabla Q_{ij}} = 0 \quad \text{(bulk)}, \quad (17)$$

$$\frac{\partial f}{\partial \nabla Q_{ij}} \cdot \boldsymbol{\nu} = 0 \quad \text{(surface)}. \quad (18)$$

Here, $\boldsymbol{\nu}$ is the surface normal. Applying the above formalism for the most commonly used LdG free energy density f_{LdG} (Equation (9)) and Rapini–Papoular-like surface free energy $f_{\text{surf}}^{\text{uni}}$ (Equation (14)) yields

$$h_{ij}^{\text{bulk}} \equiv L\nabla^2 Q_{ij} - AQ_{ij} - BQ_{ik}Q_{kj} - CQ_{ij}(Q_{kl}Q_{lk}) = 0, \quad (19)$$

$$h_{ij}^{\text{surf}} \equiv L\frac{\partial Q_{ij}}{\partial x_k}\nu_k + W(Q_{ij} - Q_{ij}^0) = 0, \quad (20)$$

where Equation (19) determines the bulk behaviour and Equation (20) determines the homeotropic surface behaviour of the component Q_{ij}. Here h_{ij}^{bulk} and h_{ij}^{surf} are referred to as molecular fields, and $A = a\,(T - T_{NI}^*)$. We avoid detailed quantitative modelling of materials, therefore in the following we use a single elastic constant (L) approximation. The equilibrium profile of the order parameter tensor Q_{ij} is found by solving the above set of six coupled non-linear bulk nematic equations (one for each independent component of Q_{ij}) with proper boundary conditions (e.g. Equation (20)). This is done numerically by using an explicit relaxation algorithm on a cubic mesh. Note that in principle six coupled equations can be reduced to five by taking into account the condition $trQ_{ij} = 0$, but this typically severely reduces the stability of the numerical scheme.

The relaxation algorithm assigns an additional relaxation coordinate t (which can be interpreted as time) to the order parameter tensor. The coordinate t characterises the iterative evolution of the order parameter tensor profile from the initial configuration to a finite equilibrium state. Having Q_{ij} dependent both on the position vector $\mathbf{r}$ and t ($Q_{ij} = Q_{ij}(\mathbf{r}, t)$), the

molecular field (Equations (19) and (20)) is extended by an explicit derivative with respect to t when applying the EL formalism:

$$\Gamma \frac{\mathrm{d}Q_{ij}}{\mathrm{d}t} = h_{ij}^{\cdots}, \tag{21}$$

where Γ is a numerical relaxation constant and $h_{ij}^{\cdots}$ denotes h_{ij}^{bulk} or h_{ij}^{surf}. By discretising (21) in time and introducing an explicit iteration scheme one obtains:

$$Q_{ij}^{t+\Delta t} = Q_{ij}^{t} + \frac{\Delta t}{\Gamma} h_{ij}^{\cdots t}. \tag{22}$$

Here Δt is the time interval between two sequent iteration steps. The number of iteration steps is highly dependent on the initial configuration and size of the system (the number of mesh points) but typically ranges from 1000 to 100,000.

The order parameter tensor Q_{ij} is spatially discretised on a cubic mesh with either uniform or variable mesh density. The variable mesh is finer in the regions populated by particles but coarser in the surroundings. Resolution of the finer mesh Δx is determined according to the nematic correlation length ξ_{N}. Empirically we have found that for $\xi_{\mathrm{N}}/\Delta x \lesssim 0.7$, relaxation of the nematic degree of order S within Q_{ij} is ensured (no defect-pinning), whereas for $\xi_{\mathrm{N}}/\Delta x \gtrsim 1$, only tensor profiles with constant S can be modelled. To maximise the physical size of the simulation box, a mesh with variable mesh density is often used for systems where an 'empty' nematic cell is modelled and the effect of the side surfaces is to be minimised (see Figure 2(a)). The finer internal mesh has a resolution which allows modelling with a varying degree of order, whereas at the external mesh only elastic distortions with a constant S have to be ensured.

All mesh points are assigned logical markers which characterise their role (their governing equation) within the calculations. Three categories of logical markers are introduced: bulk, surface and particle interior. Bulk points obey relaxation equations with h_{ij}^{bulk}, surface points use h_{ij}^{surf}, whereas at the particle points $Q_{ij} = 0$. In order to introduce the surface of a spherical particle located at $(x_{col}, y_{col}, z_{col})$ with the radius r_c, a criterion is introduced for logical markers which separates bulk, surface and particle interior as

$$\mathrm{logicalmarker} = \begin{cases} \text{particle} & \text{if } \dfrac{(x-x_{\mathrm{col}})^2}{(r_c-\Delta x/2)^2} + \dfrac{(y-y_{\mathrm{col}})^2}{(r_c-\Delta y/2)^2} + \dfrac{(z-z_{\mathrm{col}})^2}{(r_c-\Delta z/2)^2} < 1 \\ \text{surface} & \text{if } \dfrac{(x-x_{\mathrm{col}})^2}{(r_c-\Delta x/2)^2} + \dfrac{(y-y_{\mathrm{col}})^2}{(r_c-\Delta y/2)^2} + \dfrac{(z-z_{\mathrm{col}})^2}{(r_c-\Delta z/2)^2} \geq 1 \\ & \text{and } \dfrac{(x-x_{\mathrm{col}})^2}{(r_c+\Delta x/2)^2} + \dfrac{(y-y_{\mathrm{col}})^2}{(r_c+\Delta y/2)^2} + \dfrac{(z-z_{\mathrm{col}})^2}{(r_c+\Delta z/2)^2} < 1 \\ \text{bulk} & \text{otherwise.} \end{cases}$$

The logical marker allocation is presented graphically in Figure 2(b), where the white background colour represents bulk, the light grey the surface and the dark grey the interior of the particles.

The parameter values in the following numerical calculations correspond roughly to 5CB nematic liquid crystal and strong homeotropic surface anchoring. The following values are used if not stated differently: $L = 4 \times 10^{-11}$N, $A = -0.172 \times 10^6 \mathrm{Jm}^{-3}$, $B = -2.12 \times 10^6 \mathrm{Jm}^{-3}$, $C = 1.73 \times 10^6 \mathrm{Jm}^{-3}$, particle diameter $d = 2r_c = 1\mu$m, cell thickness $h = 2\mu$m, homeotropic anchoring strength $W^{\mathrm{uni}} = 1 \times 10^{-2} \mathrm{Jm}^{-2}$, and mesh resolution (cubic mesh) $\Delta x = 10$nm. These parameters give $\xi_{\mathrm{N}} = 6.63$nm and $S_{\mathrm{eq}} = 0.533$.

3. Colloidal structures

The numerical modelling using LdG free energy minimisation is illustrated with examples of colloidal

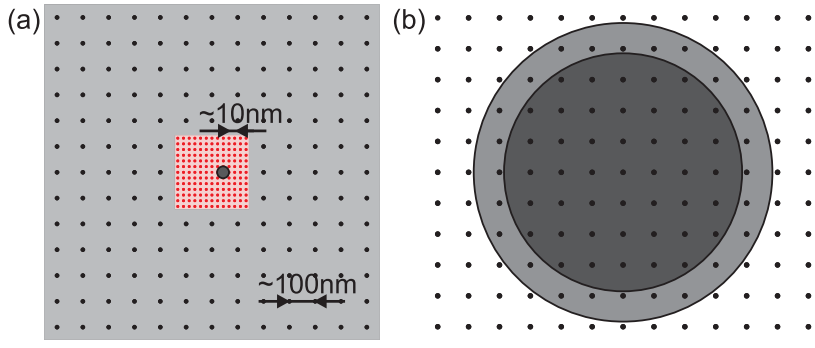

Figure 2. (a) Mesh with variable mesh density: the inner finer mesh (in red) enables full detailed calculation with the order parameter tensor, whereas the coarser mesh (in black) allows only elastic (Frank's) deformations of the tensor. (b) Allocation of the particle surface: particle interior (dark grey), surface (light grey) and bulk (white). Colour refers to the online version.

structures. We show colloidal particles with director fields characterised by elastic dipolar, quadrupolar and dipolar–quadrupolar director configurations, entangled dimer and dimer bound by an escaped hyperbolic ring, referred to also as 'bubble gum'.

3.1 Single particles

Single micrometre particles with homeotropic surfaces form director fields characterised either by elastic dipoles or quadrupoles. Which of the two possible structures is stable and which is metastable depends primarily on particle size, surface anchoring strength, confinement and external field. In Figure 3, homeotropic particles ($d = 2\mu$m) surrounded by a dipolar and quadrupolar director structure are presented. Defects are characterised by the depression of order as was illustrated in Figure 1. Therefore, one can visualise them by simply tracing a chosen value of the order parameter. We chose visualisation via isosurfaces of a selected constant value of the nematic degree of order S.

The hyperbolic −1 point defect of the dipolar configuration opens into a small defect ring which is characterised by the winding number $-1/2$ (see (*61*)). The LdG free energy namely minimises by transforming the point defect into a small ring (*62–64*). The position of the hyperbolic defect is at $1.23r_c$ which is in good agreement with results from Lubensky *et al.* ($1.19r_c$; multipole expansion (*39*)). For the elastic quadrupole we find the Saturn ring at $1.15r_c$. Lubensky *et al.* (*39*) found the position of the defect ring at $1.08r_c$, whereas Kuksenok *et al.* (*65*) reported $1.25r_c$.

To ensure that in the calculations the dipolar director configuration forms around the particle and to speed up the relaxation process, calculations are started from a specific initial condition. For the initial condition in the close surroundings of the particle, the tensor profile is chosen to have its director component as obtained from a multipole expansion (*9*):

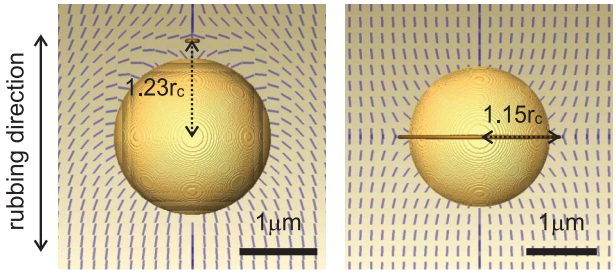

Figure 3. Spherical beads in a nematic liquid crystal: elastic dipole (left), elastic quadrupole (right). For defect visualisation we choose an isosurface with $S = 0.48$. The top view on the planar cell is presented. The thickness of the planar cell $h = 3\mu$m.

$$\mathbf{n} = \mathbf{e}_z \pm Pr_c^2 \frac{\mathbf{r} - \mathbf{r}_{\mathrm{col}}}{|\mathbf{r} - \mathbf{r}_{\mathrm{col}}|^3}, \tag{23}$$

where $\mathbf{e}_z$ is a unit vector pointing along the far-field director, P is the constant which determines the initial position of the point defect (we have used $P = 2.08$), $\mathbf{r}_{\mathrm{col}}$ is the position of the colloidal particle, $\mathbf{r}$ is the position vector, and by switching plus and minus one controls the orientation of the elastic dipole. Note that Equation (23) has to be normalised if used at positions close to the particle. For particles smaller than a few hundred nanometres, the dipolar configuration is energetically highly unfavourable in comparison to the quadrupolar configuration (*9*) and becomes unstable.

Calculations of the quadrupolar nematic configuration are started from a uniform initial tensor configuration, corresponding to the uniform spatially independent director field **n**. We observe that by starting from a uniform orientation, the Saturn-ring defect gradually starts to form at the equator of the particle in the plane perpendicular to **n** at the very beginning of our calculations. The defect first lies at the surface of the particle, but if the anchoring is strong enough, it quickly (within few hundred explicit iteration steps) detaches from the surface and forms a real ring. By changing the direction of initial uniform director around a particle, one can also control the initial orientation of the Saturn-ring defect, as it always lies in the plane perpendicular to **n**.

3.2 Dipolar and quadrupolar dimers

The interaction between elastic dipoles and quadrupoles is anisotropic. A pair of elastic dipoles has two different stable configurations in a uniform nematic field. Two antiparallel dipoles attract one another sideways, as two parallel dipoles form a linear chain. A quadrupolar dimer has one sideways stable configuration. Particles attract one another at an angle of 79° with respect to the far-field director.

Binary mixtures of elastic dipoles and quadrupoles can be experimentally realised at suitable cell thicknesses of approximately $1.5d$ (see (*20*)). At such 'intermediate' confinement the (meta)stable dipolar and quadrupolar configurations become energetically comparable and thus coexist. This mixed type of director field symmetry results in a new complex interparticle potential which allows a broad variety of new binary colloidal crystals to be built in two dimensions.

A pair of dipolar and quadrupolar particles has three stable equilibrium configurations. Figure 4(a) shows a configuration where the dipolar colloidal particle is attracted directly along the director to the quadrupolar colloidal particle. The pair shares the

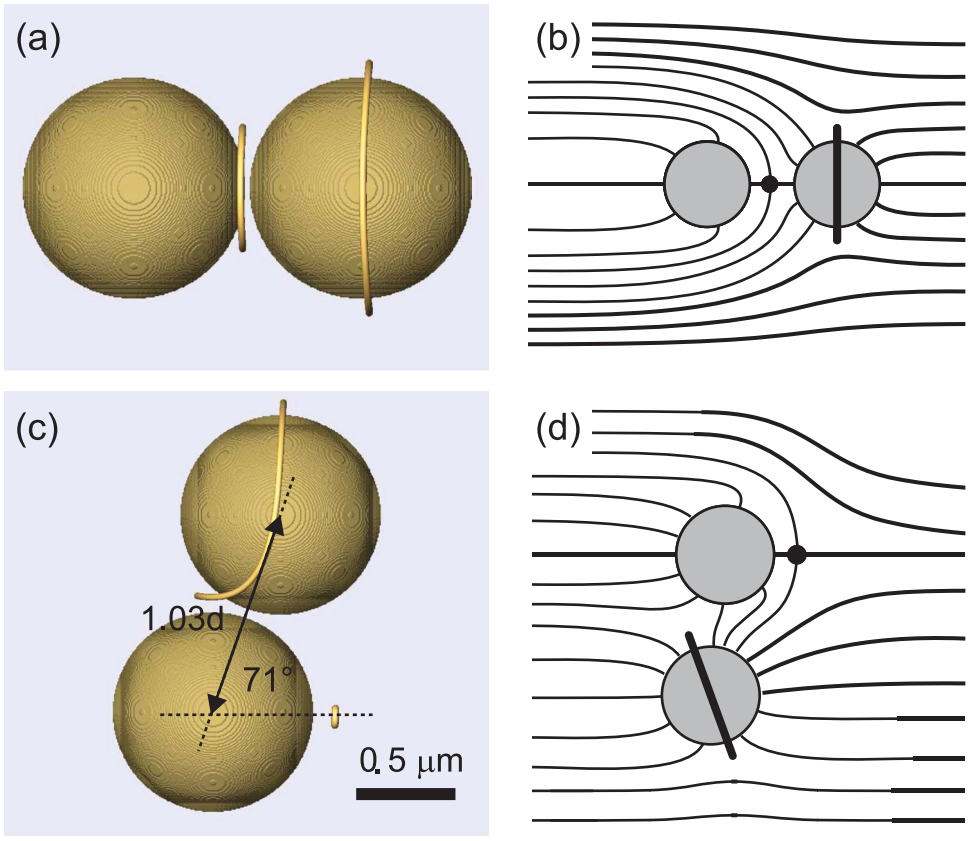

Figure 4. (a) A pair of dipole–quadrupole particles, attracted along the director and (b) the corresponding director field. (c) Dipole–quadrupole pair, attracted sideways and (d) the corresponding director field.

hyperbolic hedgehog point defect, which lies in between them as shown schematically in Figure 4(b). The two additional stable configurations are symmetric with respect to each other. One of the configurations is shown in Figure 4(c) with the scheme of the corresponding director in Figure 4(d). Here, the elastic dipole is attracted to the quadrupole at a certain angle with respect to far-field director. We find that the interparticle separation is equal to $1.03d$ and the relative angle of the pair with respect to the director is 71°. One can see that for the linear pair along the director, the hyperbolic point defect has opened due to confinement into a small ring as already observed in the dipolar 2D crystals. Interestingly, in the sideways pair configuration the quadrupolar defect ring is strongly bent.

From a large number of different mixed colloidal crystals we focused on the most dense colloidal structure. The results (see Figure 5) reveal that defect rings in such 2D binary colloidal configurations can be highly deformed (see Figure 5(a)). In general, binary 2D colloidal crystals have lower symmetry than the simple 'only-dipolar' and 'only-quadrupolar' crystals. The unit cell size and number of particles within a unit cell is therefore typically larger compared with simple crystals. Modelling of such crystallites is more demanding and time consuming. In addition to the increased unit cell size, additional particle position parameters have to be minimised. The spatial dependence of two such parameters, particle positions I and J, for the most dense binary crystal is presented in Figure 5.

3.3 *Entangled dimers*

Liquid crystals around colloidal particles adopt a variety of different configurations with the same external parameters, such as confinement, external fields, surface anchoring and particle size. Nevertheless, the absolute stability of various colloidal structures depends on their total free energy. All stable or metastable structures are characterised by a local minima in the free energy profile where the exact value of their total free energy determines their stability or metastability. Energy barriers between the structures are typically much larger than k_BT; therefore thermal

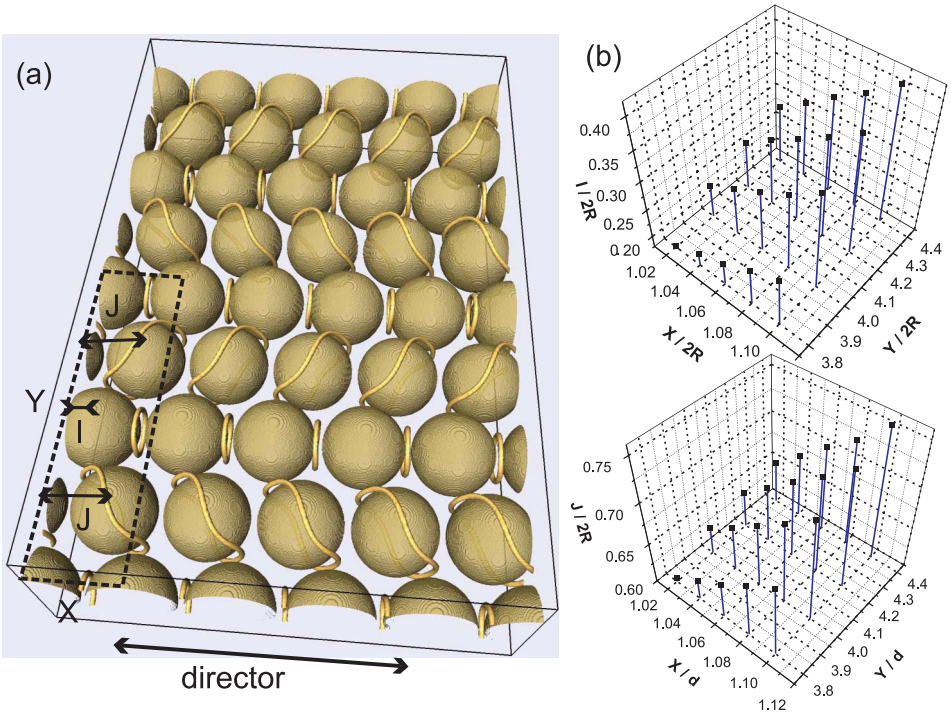

Figure 5. Mixed dipolar–quadrupolar 2D colloidal crystals. (a) The stable configuration of the most dense mixed 2D colloidal crystal. Dashed lines show the 2D unit cell. (d) Particle positions I and J as a function of lattice constants X and Y.

fluctuations are insufficient to trigger structural transitions. Using numerical calculations we were able to predict new nematic colloidal structures bound by delocalised defect loops (*38*, *66*). Temperature quench from the isotropic to the nematic phase is used as a procedure to find such entangled assemblies. Nanoscale studies of related structures were discussed elsewhere (*36*, *55*, *67–69*)

The probability of finding a particular colloidal structure depends primarily on its total free energy but also on external parameters, such as the material flow, temperature profile, domain walls and kinetics of defects. The external parameters can energetically favour a particular colloidal structure during its formation. In general, the energy scale of nematic colloids far exceeds k_BT, and so the frequency of occurrence of a particular configuration is not determined by the Boltzmann distribution. The relative frequency of a pair of structures does not depend solely on the difference of their total free energies. This must be borne in mind when building complex colloidal superstructures.

Directed formation of particular structures is achieved or avoided in numerical calculations by choosing suitable initial conditions. To generate elastic dipoles and quadrupoles we had to use suitable Ansatz functions. A limitation of the free energy minimisation method is that it finds only one (meta)stable configuration of the nematic around the colloidal particles for a given initial nematic configuration. A more general way is to use random orientations (spins) at all mesh points in the starting configuration, since such a completely disordered nematic state helps to avoid energy barriers between the configurations and can access solutions in these additional local free energy minima.

When performing a sudden isotropic-to-nematic transition, the phenomenon of entanglement is observed in nematic colloids. Defects are unable to relax completely since they are hindered by the presence of particles. Therefore, metastable configurations can arise where complex defect loops entangle several colloidal particles. Three types of entangled dimers are found: 'figure of eight', 'figure of omega' and 'entangled point defect'. A particle dimer bound by a figure of eight defect structure is shown in Figure 6(a), with the local profile of the director in the intermediate region between the particles presented in Figure 6(b). For details see (*38*) and (*66*).

The figure of eight structure (Figure 6) is stabilised by a single $-1/2$ hyperbolic disclination line. The disclination line starts at the top of the first particle, sinks below the second, comes from behind to the top of the second, sinks below the first, and finally from behind of the first particle connects into a loop. The disclination line makes a 'figure of eight'

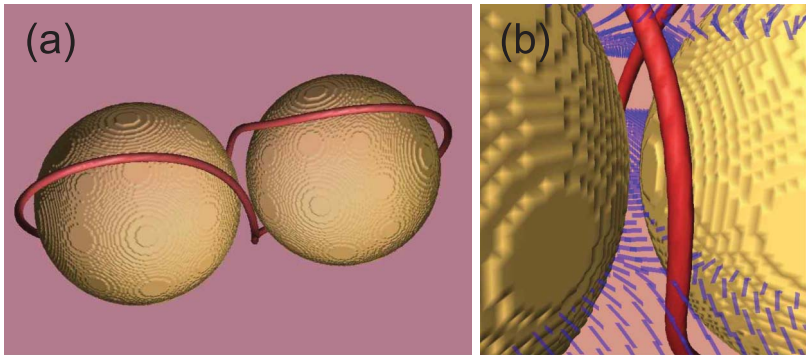

Figure 6. (a) Colloidal dimer entangled by the figure of eight defect structure. (b) Local director profile. Defect loop (in red) is visualised by drawing isosurfaces of the nematic degree of order $S = 0.48$. Thin lines (in blue) show the local director. Colour refers to the online version.

if observed from the side (along the far-field director). In contrast to the figure of eight, the figure of omega (*66*) has a straight defect line at the front side, which sinks behind both colloidal particles and makes an additional loop in between them. This additional loop resembles a Greek letter Ω if viewed along the particle dimer. The entangled point defect structure (*66*) consists of two separate $-1/2$ defect rings, which are oriented perpendicular with respect to each other. The larger defect ring winds around both particles and stabilises them into a stable entangled object. The inner smaller ring is effectively a -1 hyperbolic point defect with an escaped core. In terms of entanglement, it is a 'bystander' as it only locally relaxes the director field.

Figure of eight and figure of omega are chiral objects as they break the mirror symmetry. The structures with left or right handedness are equally probable and have the same free energy. The degeneracy of the two structures can be lifted by using a non-homogeneous preferential nematic ordering (e.g. the $\pi/2$ cell). Observing such spontaneous formation of chiral objects in an achiral medium is highly interesting and could be exploited for applications in optics.

3.4 Dimers with escaped hyperbolic loops

Structures with escaped hyperbolic defect rings have a non-singular director which is achieved by topological point defects escaping into defect rings. In the literature, they are also referred to as the bubble-gum structures (*39*, *70*, *71*). In the geometry of a uniform planar cell, these structures are rather metastable with respect to elastic dipoles (*71*) or quadrupoles and are very unlikely to form.

An interesting aspect of the escaped hyperbolic defect rings is how to characterise their shape and position. The spatial variations in the nematic degree of order S within the escaped cores of these defect rings are typically smaller than 2% (bulk $S_{eq} = 0.533$) which makes them inadequate for defect position analysis. Therefore, we introduce a geometrical escape parameter $\tilde{S}$ to draw centres of the escaped defect rings. The parameter $\tilde{S}$ is given by (*72*):

$$\tilde{S} = 1 - |\mathbf{n} \cdot \mathbf{e}_{\perp}| - |\mathbf{n} \cdot \mathbf{n}_0|, \tag{24}$$

where $\mathbf{e}_{\perp} = [\mathbf{r} - (\mathbf{r} \cdot \mathbf{e})\mathbf{e}]/|\mathbf{r} - (\mathbf{r} \cdot \mathbf{e})\mathbf{e}|$, $\mathbf{n}_0 = (1, 0, 0)$ is the far-field director, $\mathbf{r}$ position vector and $\mathbf{e}$ unit vector along the dimer. The isosurface of $\tilde{S} \sim 1$ draws centres of escaped hyperbolic defect rings with a precision of the order of mesh resolution.

Figure 7(a) shows a dimer bound by an escaped hyperbolic ring in a uniform planar cell. The structure was calculated using a guess for the initial condition of the numerical relaxation. This was the Ansatz function for the defect ring (*72*), and, as suggested by Fukuda and Yokoyama (*71*), two antiparallel elastic dipoles for the remaining director profile. The local profile of the director within the escaped hyperbolic ring is presented in Figure 7(b). One can observe the effective escape of the hyperbolic defect ring in two perpendicular planes which generates a local twist deformation. Topologically, such an escaped defect loop is homotopic to a point defect with topological charge of magnitude two. Locally, the winding number -1 can be attributed to the line of the escaped hyperbolic ring.

3.5 Hierarchical saturn-ring superstructure

In materials science, hierarchy is an interesting phenomenon where material parameters at a given larger scale control the material response at a different smaller scale. Scale refers typically to either the energy or physical size of the system but can be generalised to almost any physical quantity. Liquid crystal colloids are systems which can be ordered hierarchically. By

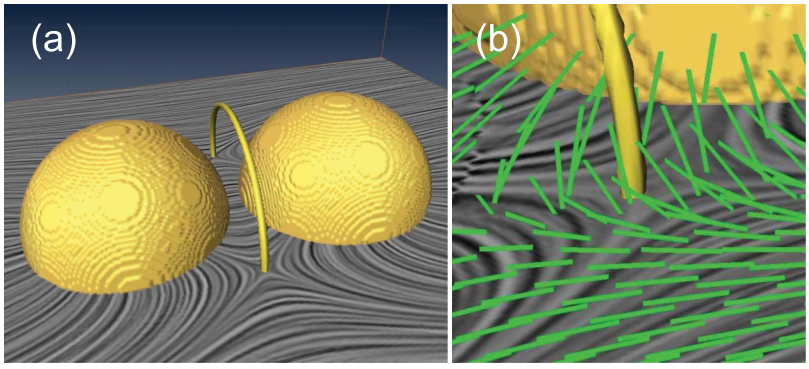

Figure 7. (a) Particle dimer bound by an escaped hyperbolic defect ring, also referred to as a 'bubble-gum defect'. Grey streamlines show the projection of the director on the given plane to visualise the true –1 hyperbolic nature of the escaped line. (b) Director profile (in green) shows the escape into the third dimension in the centre of the hyperbolic ring. Colour refers to the online version.

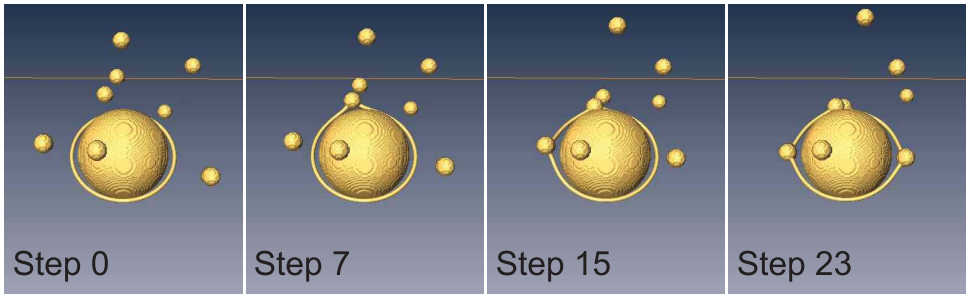

Figure 8. Hierarchical Saturn-ring superstructure. Smaller 100nm particles are trapped in the disclination loop of a Saturn-ring defect, that has formed around a larger particle with diameter of 1μm. Step 0 corresponds to the initial configuration. Further steps correspond to the relaxational evolution obtained by using our quasi-dynamics of the system. Disclination loops are visualised by isosurfaces of the scalar order parameter being $S = 0.45$ ($S_{eq} = 0.533$).

using colloidal particles of different sizes, i.e. length scales, and nematic-induced elastic potential between particles, we build colloidal superstructures where larger particles generate nematic profile which controls the assembly of smaller-scale particles.

To demonstrate modelling of the hierarchical ordering, we focus on a single larger spherical particle with homeotropic anchoring that spontaneously generates a Saturn-ring defect loop at the equator. Bringing a smaller colloidal particle close to the Saturn ring, the interaction becomes non-zero. The attraction is locally equivalent as in the case of approaching a straight $-1/2$ disclination line. The main conceptual difference is however that it is the larger colloidal particle that at its own scale generates the Saturn ring which then builds an effective potential for smaller particles and thus controls their assembly at another smaller scale. Such a hierarchical ladder has no limitation for including more that two particle scales (sizes). Figure 8 presents several steps in the numerical trapping of small colloidal particles into the Saturn ring of a larger colloidal particle. For further details and for matching to the experimental observations, the interested reader is referred to (*3*).

4. Conclusions

The LdG modelling of nematic liquid crystal colloids based on the nematic order parameter tensor has been reviewed. Basic free energy contributions compulsory for modelling of nematic colloids have been limited to gradient of order, nematic phase, and surface anchoring terms. Free energy has been minimised by using an EL formalism to obtain the governing equations for the nematic profile in bulk and at the surface. A numerical finite difference relaxation scheme has been presented together with the particle allocation. Examples of colloidal structures were shown next. Starting from single elastic dipoles and quadrupoles, we assembled combined dipolar–quadrupolar dimers. Two stable configurations were found. As an example of entangled

structures, we showed a dimer bound by the figure of eight defect structure which proves to be a new highly robust chiral colloidal object. A dimer bound by an escaped hyperbolic ring was calculated. Here, a non-singular director stabilises the colloidal configuration and again builds a new topological structure. Finally, a hierarchical assembly of smaller sub-micrometre particles into a Saturn ring of a larger micrometre-sized particle was shown, to demonstrate that the LdG modelling can be applied to multi-scale multi-particle close-packed colloidal system.

The LdG free energy minimisation approach has, in combination with various numerical techniques, strong explanatory and predictive power. All presented examples of colloidal structures have their experimental realisations, and very often not only qualitative but also quantitative mapping between the modelling and experiments can be found. The approach can be applied to a large range of scales, highly complex geometries, chiral structures, patterned particles, ferroelectric and ferromagnetic particles, complex external fields, and the model always retains an elementary phenomenological interpretation. LdG modelling is therefore an important element in the theoretical science of liquid crystal colloids.

References

(1) de Gennes, P.G.; Prost, J. *The Physics of Liquid Crystals*, 2nd Ed.; Oxford Science Publications: Oxford, 1993.
(2) Onsager, L. *Ann. N. Y. Acad. Sci.* **1949**, *51*, 627–659.
(3) Skarabot, M.; Ravnik, M.; Zumer, S.; Tkalec, U.; Poberaj, I.; Babic, D.; Musevic, I. *Phys. Rev. E* **2008**, *77*, 061706.
(4) Pires, D.; Fleury, J.-B.; Galerne, Y. *Phys. Rev. Lett.* **2007**, *98*, 247801.
(5) Whitesides, G.M.; Grzybowski, B. *Science* **2002**, *295*, 2418–2421.
(6) Vlasov, Y.A.; Bo, X.-Z.; Sturm, J.C.; Norris, D.J. *Nature* **2001**, *414*, 289–293.
(7) Smith, D.R.; Pendry, J.B.; Wiltshire, M.C.K. *Science* **2004**, *305*, 788–792.
(8) Jérôme, B. *Rep. Prog. Phys.* **1991**, *54*, 391–451.
(9) Stark, H. *Phys. Rep.* **2001**, *351*, 387–474.
(10) Gu, Y.; Abbott, N.L. *Phys. Rev. Lett.* **2000**, *85*, 4719–4722.
(11) Stark, H. *Phys. Rev. E* **2002**, *66*, 032701.
(12) Cladis, P.; Kleman, M.; Pieranski, P. *C. R. Acad. Sci. Paris* **1971**, *273*, 275.
(13) Poulin, P.; Stark, H.; Lubensky, T.C.; Weitz, D.A. *Science* **1997**, *275*, 1770–1773.
(14) Loudet, J.C.; Barois, P.; Poulin, P. *Nature* **2000**, *407*, 611–613.
(15) Poulin, P.; Weitz, D.A. *Phys. Rev. E* **1998**, *57*, 626–637.
(16) Yada, M.; Yamamoto, J.; Yokoyama, H. *Phys. Rev. Lett.* **2004**, *92*, 185501.
(17) Loudet, J.C.; Barois, P.; Auroy, P.; Keller, P.; Richard, H.; Poulin, P. *Langmuir* **2004**, *20*, 11336–11347.
(18) Musevic, I.; Skarabot, M.; Tkalec, U.; Ravnik, M.; Zumer, S. *Science* **2006**, *313*, 954–958.
(19) Musevic, I.; Skarabot, M. *Soft Matter* **2008**, *4*, 195–199.
(20) Ognysta, U.; Nych, A.; Nazarenko, V.; Musevic, I.; Skarabot, M.; Ravnik, M.; Zumer, S.; Poberaj, I.; Babic, D. *Phys. Rev. Lett.* **2008**, *100*, 217803.
(21) Nazarenko, V.G.; Nych, A.B.; Lev, B.I. *Phys. Rev. Lett.* **2001**, *87*, 075504.
(22) Smalyukh, I.I.; Chernyshuk, S.; Lev, B.I.; Nych, A.B.; Ognysta, U.; Nazarenko, V.G.; Lavrentovich, O.D. *Phys. Rev. Lett.* **2004**, *93*, 117801.
(23) Nych, A.B.; Ognysta, U.M.; Pergamenshchik, V.M.; Lev, B.I.; Nazarenko, V.G.; Musevic, I.; Skarabot, M.; Lavrentovich, O.D. *Phys. Rev. Lett.* **2007**, *98*, 057801.
(24) Zapotocky, M.; Ramos, L.; Poulin, P.; Lubensky, T.C.; Weitz, D.A. *Science* **1999,** *283*, 209–212.
(25) Lapointe, C.; Hultgren, A.; Silevitch, D.M.; Felton, E.J.; Reich, D.H.; Leheny, R.L. *Science* **2004**, *303*, 652–655.
(26) Tatarkova, S.A.; Burnham, D.R.; Kirby, A.L.; Love, G.D.; Terentjev, E.M. *Phys. Rev. Lett.* **2007,** *98*, 157801.
(27) Revol, J.F.; Bradford, H.; Giasson, J.; Marchessault, R.H.; Gray, D.G. *Int. J. Biol. Macromol.* **1992**, *14*, 170–172.
(28) Mertens, G.; Roder, T.; Schweins, R.; Huber, K.; Kitzerow, H.S. *Appl. Phys. Lett.* **2002**, *80*, 1885–1887.
(29) Musevic, I.; Skarabot, M.; Babic, D.; Osterman, N.; Poberaj, I.; Nazarenko, V.; Nych, A. *Phys. Rev. Lett.* **2004**, *93*, 187801.
(30) Kotar, J.; Vilfan, M.; Osterman, N.; Babic, D.; Copic, M.; Poberaj, I. *Phys. Rev. Lett.* **2006**, *96*, 207801.
(31) Luckhurst, G.R.; Stephens, R.A.; Phippen, E.W. *Liq. Cryst.* **1990**, *8*, 451–464.
(32) Lebwohl, P.A.; Lasher, G. *Phys. Rev. A.* **1972**, *6*, 426–429.
(33) Smondyrev, A.M.; Pelcovits, R.A. *Liq. Cryst.* **1999**, *26*, 235–240.
(34) Skacej, G.; Zannoni, C. *Phys. Rev. Lett.* **2008**, *100*, 197802.
(35) Press, W.H.; Flannery, B.P.; Teukolsky, S.A.; Vetterling, W.T. *Numerical Recipes*; Cambridge University Press: Cambridge, 1986.
(36) Araki, T.; Tanaka, H. *Phys. Rev. Lett.* **2006**, *97*, 127801.
(37) Denniston, C.; Orlandini, E.; Yeomans, J.M. *Phys. Rev. E* **2001**, *63*, 056702.
(38) Ravnik, M.; Skarabot, M.; Zumer, S.; Tkalec, U.; Poberaj, I.; Babic, D.; Osterman, N.; Musevic, I. *Phys. Rev. Lett.* **2007**, *99*, 247801.
(39) Lubensky, T.C.; Pettey, D.; Currier, N.; Stark, H. *Phys. Rev. E* **1998**, *57*, 610–625.
(40) Tanaka, H.; Araki T. *Phys. Rev. Lett.* **2000**, *85*, 1338–1341.
(41) Smith, C.J.; Denniston C. *J. Appl. Phys.* **2007**, *101*, 014305.
(42) Dupuis, A.; Marenduzzo, D.; Orlandini, E.; Yeomans, J.M. *Phys. Rev. Lett.* **2005**, *95*, 097801.
(43) Alexander, G.P.; Yeomans, J.M. *Phys. Rev. E* **2006**, *74*, 061706.
(44) Mermin, N.D. *Rev. Mod. Phys.* **1997**, *51*, 591–648.
(45) Allender, D.; Longa, L. *Phys. Rev. E* **2008**, *78*, 011704.
(46) Chen, G.P.; Takezoe, H.; Fukuda, A. *Liq. Cryst.* **1989**, *5*, 341–347.
(47) de Gennes, P.G. *Mol. Cryst. Liq. Cryst.* **1971**, *12*, 193–214.
(48) Lubensky, T.C. *Phys. Rev. A* **1970**, *2*, 2497–2514.

(49) Schiele, K.; Trimper, S. *Phys. Status Solidi B* **1983**, *118*, 267–274.
(50) Crawford, G.P.; Doane, J.W.; Zumer, S. Polymer Dispersed Liquid Crystals: Nematic Droplets and Related Systems. In *Handbook of Liquid Crystal Research*; Collings, P.J. and Patel, J.S., Eds.; Oxford University Press: New York, 1997.
(51) Pelka, R.; Saito, K. *Phys. Rev. E* **2006**, *74*, 041705.
(52) Barbero, G.; Durand, G. *Phys. Rev. E* **1993**, *48*, 1942–1947.
(53) Crawford, G.P.; Allender, D.W.; Doane, J.W. *Phys. Rev. A* **1992**, *45*, 8693–8708.
(54) Wright, D.C.; Mermin, N.D. *Rev. Mod. Phys.* **1989**, *61*, 385–432.
(55) Guzman, O.; Kim, E.B.; Grollau, S.; Abbott, N.L.; de Pablo, J.J. *Phys. Rev. Lett.* **2003**, *91*, 235507.
(56) De Lozar, A.; Schopf, W.; Rehberg, I.; Svensek, D.; Kramer, L. *Phys. Rev. E* **2005**, *72*, 051713.
(57) Blinov, L.; Kabayankov, A.; Sonin, A. *Liq. Cryst.* **1989**, *5*, 645–661.
(58) Fournier, J.B.; Galatola, P. *Europhys. Lett.* **2005**, *72*, 403–409.
(59) de Gennes, P.G. *The Physics of Liquid Crystals*; Oxford Science Publications: Oxford, 1974.
(60) Kleman, M.; Williams, C. *Phil. Mag.* **1973**, *28*, 725–731.
(61) Trebin, H.-R. *Adv. Phys.*, **1982**, *31*, 195–254.
(62) Penzenstadler, E.; Trebin, H.-R. *J. Phys. France* **1989**, *50*, 1027–1040.
(63) Mkaddem, S.; Gartland, E.C. *Phys. Rev. E* **2000**, *62*, 6694–6705.
(64) Chiccoli, C.; Pasini, P.; Semeria, F.; Sluckin, T.J.; Zannoni, C. *J. Phys. II* **1995**, *5*, 427–436.
(65) Kuksenok, O.V.; Ruhwandl, R.W.; Shiyanovski, S.V.; Terentjev, E.M. *Phys. Rev. E* **1996**, *54*, 5198–5203.
(66) Ravnik, M.; Zumer, S. *Soft Matter* **2009**, *5*, 269–274.
(67) Kim, E.B.; Guzman, O.; Grollau, S.; Abbott, N.L.; de Pablo, J.J. *J. Chem. Phys.* **2004**, *121*, 1949–1961.
(68) Hung, F.R.; Guzman, O.; Gettelfinger, B.T.; Abbott, N.L.; de Pablo, J.J. *Phys. Rev. E* **2006**, *74*, 011711.
(69) Hung, F.R. *Phys. Rev. E* **2009**, *79*, 021705.
(70) Poulin, P.; Cabuil, V.; Weitz, D.A. *Phys. Rev. Lett.* **1997**, *79*, 4862–4865.
(71) Fukuda, J.; Yokoyama, H. *Phys. Rev. Lett.* **2005**, *94*, 148301.
(72) Tkalec, U.; Ravnik, M.; Zumer, S.; Musevic, I. Broken mirror symmetry in nematic colloids: chiral dimers and 2D crystals. *Phys. Rev. Lett.*, submitted.